arXiv:1212.1840v1 [physics.ins-det] 8 Dec 2012

The Polarized H and D Atomic Beam Source for ANKE at COSY-Jülich[a)]

M. Mikirtychyants,[1, 2, b)] R. Engels,[1] K. Grigoryev,[1, 2] H. Kleines,[3] P. Kravtsov,[2] S. Lorenz,[4, c)] M. Nekipelov,[1, 2, d)] V. Nelyubin,[2, e)] F. Rathmann,[1] J. Sarkadi,[1] H. Paetz gen. Schieck,[5] H. Seyfarth,[1] E. Steffens,[4] H. Ströher,[1] and A. Vasilyev[2]
[1)] *Institut für Kernphysik, Forschungszentrum Jülich, 52425 Jülich, Germany*
[2)] *High Energy Physics Department, St.Petersburg Nuclear Physics Institute, 188300 Gatchina, Russia*
[3)] *Zentrallabor für Elektronik, Forschungszentrum Jülich, 52425 Jülich, Germany*
[4)] *Physikalisches Institut, Friedrich-Alexander-Universität Erlangen-Nürnberg, 91058 Erlangen, Germany*
[5)] *Institut für Kernphysik, Universität zu Köln, 50937 Köln, Germany*

(Dated: 11 December 2012)

A polarized atomic beam source was developed for the polarized internal storage-cell gas target at the magnet spectrometer ANKE of COSY-Jülich. The intensities of the beams injected into the storage cell, measured with a compression tube, are $7.5 \cdot 10^{16}$ hydrogen atoms/s (two hyperfine states) and $3.9 \cdot 10^{16}$ deuterium atoms/s (three hyperfine states). For the hydrogen beam the achieved vector polarizations are $p_{\mathrm{z}} \approx \pm 0.92$. For the deuterium beam, the obtained combinations of vector and tensor (p_{zz}) polarizations are $p_{\mathrm{z}} \approx \pm 0.90$ (with a constant $p_{\mathrm{zz}} \approx +0.86$), and $p_{\mathrm{zz}} = +0.90$ or $p_{\mathrm{zz}} = -1.71$ (both with vanishing p_{z}). The paper includes a detailed technical description of the apparatus and of the investigations performed during the development.

PACS numbers: 29.25.Pj, 24.70.+s

I. INTRODUCTION

Single-polarized experiments, making use of the polarized proton and deuteron beams of the cooler storage ring COSY-Jülich and unpolarized targets, are extended to double-polarized studies[1] by the installation of an internal polarized hydrogen or deuterium storage-cell gas target. Utilizing pure gas of polarized hydrogen or deuterium, these targets circumvent the problem of dilution by unpolarized nucleons and they permit fast change of the polarization direction. In order to compensate for the relatively low areal density, these targets are placed inside storage rings, where they are traversed by the orbiting beam typically a million times per second. As conceived already some forty years ago[2], a substantial enhancement of the areal target-gas density (or luminosity) compared to gas-jet targets by about two orders of magnitude is achieved, when the polarized atoms are injected into an open-ended, T-shaped storage cell. A review describing the capabilities of polarized gas-jet and storage-cell gas targets is found in Ref.[3].

The polarized internal target (PIT), developed for the magnet spectrometer ANKE[4] in COSY Jülich[5], consists of the polarized atomic beam source (ABS), the storage cell[6], and the Lamb-shift polarimeter (LSP)[7,8]. In the development of the PIT for ANKE the experience of other groups in the operation of polarized gas targets could be used. Essentially these are the Madison source[9], used by the PINTEX collaboration at IUCF[10,11], and the FILTEX source[12] used by the HERMES collaboration at DESY/Hamburg[13].

Section II presents the general layout of the ABS and it describes the major elements, the pumping system, the layout of the baffles, the dissociator, the nozzle-skimmer setup, the system of sextupole magnets, the high-frequency transition units, and the slow control system. Section III contains studies with the free hydrogen jet from the nozzle. In Secs. IV to VII measurements and results are presented concerning the properties of the beam behind the last magnet, the hydrogen and deuterium beam intensities (IV), hydrogen beam profiles (V), the degree of dissociation of the hydrogen beam (VI), and the polarization values for the hydrogen and deuterium beam (VII). Finally, in Sec. VIII, the conclusions and an outlook to the future efforts are given. The procedure of discharge-tube and nozzle conditioning is described in Appendix A.

II. DESCRIPTION OF THE SETUP

A. General layout of the ABS

The limited space at the target position between the first beam-bending dipole magnet D1 and the central spectrometer dipole magnet D2 of the ANKE facility[4] on

---

[a)] Work financially supported by German Ministry for Education and Research (BMBF) under contract Nos. RUS-649-96 and 06 ER 831, by Forschungszentrum Jülich (FF&E) under contract No. 41149451, by Deutsche Forschungsgemeinschaft under contract No. 436 RUS 113/430, and by the Russian Ministry of Sciences

[b)] Electronic mail: m.mikirtychyants@fz-juelich.de; Now at Institut für Experimentalphysik, Ruhr-Universität Bochum, 44801 Bochum, Germany

[c)] Now at Osram GmbH, 93049 Regensburg, Germany

[d)] Now at Wissenschaftlich-Technische Ingenieurberatung GmbH, 52428 Jülich, Germany

[e)] Now at Department of Physics, University of Virginia, Charlottesville, VA 22904, USA

the one hand enforces the ABS to be mounted in a vertical position contrary to the layout of the earlier sources. On the other hand, this position allows less complicated supports of the components and easier alignment. Furthermore, the height of the COSY tunnel restricts the vertical dimension of the ABS, which requires a very compact layout of the source. Initially, a slight inclination from the vertical ABS orientation had been foreseen to avoid drizzling of powder, created during operation of the dissociator, down into the storage cell. Production of such a powder had been observed earlier (SiO_2[14,15], "green powder"[16]). No such powder, however, was found on a glass window at the exit of the ABS in vertical position after weeks of dissociator operation. Thus, the inclination could be regarded as unnecessary.

The layout of the ABS is presented in Fig. 1. The two main cylindrical vacuum vessels are fixed above and below a central support plate. The inner diameter of the upper vessel[17] is about 390 mm. It houses the chambers I, II, and III, which are separated by two conical baffles. The dissociator tube and the coldhead[18] with the heat bridge for nozzle cooling are mounted on a three-legged plate. Three screws allow one to adjust the radial nozzle position and the distance to the skimmer.

The upper baffle between chamber I and II with the beam skimmer is rigidly connected to the upper flange of the vessel. The lower baffle with the diaphragm in front of the first sextupole magnet, separating the chambers II and III, can be moved axially from outside to optimize the pumping conditions on the one hand between the skimmer and the diaphragm, and on the other in the narrow region between the diaphragm and the front face of the first magnet. The first set of three sextupole magnets and the medium field rf transition (MFT) unit in chamber III are carried by two rods attached to the central support plate. The lower vacuum vessel, chamber IV, has a smaller inner diameter of 200 mm. It houses the second set of three sextupole magnets and a cylindrical beam chopper rotating around a horizontal axis. The separate chamber V provides space for the weak and strong field rf transition units (WFT and SFT units, respectively). The ABS can be separated from the ANKE target chamber and the COSY vacuum system by a gate valve[19] embedded by a dedicated construction into the end flange of chamber V.

Two strong turbomolecular pumps are installed at opposite flanges of chamber I perpendicular to the beam direction, one on the beam-up side of chamber II. The chambers III, IV, and V are evacuated by cryopumps. Due to space limitation around the ABS, shutters on the cryopumps as used in other sources were omitted. The gas originating from regeneration of the cryopumps is pumped via bypass tubes by turbomolecular pumps on the upper chambers. During regeneration as in other cases of pressure increase the gate valve on chamber V is closed to avoid gas flow into the ANKE target chamber.

Details of the pumping system, the baffles, the dissociator, the area around the nozzle, the magnet system,

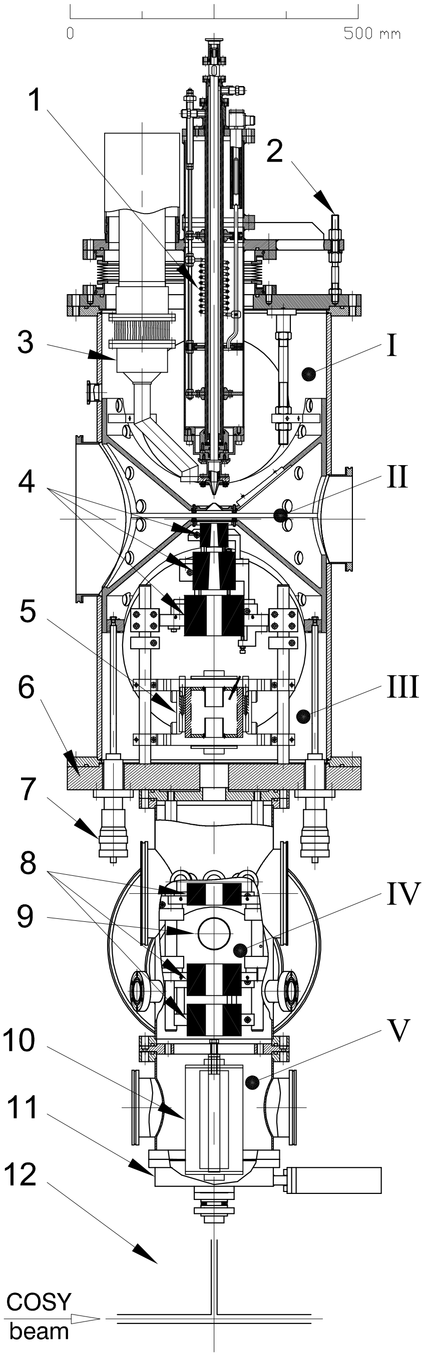

FIG. 1. Cut along the ABS axis (1: dissociator, 2: one of three adjustment screws for nozzle positioning, 3: Cu heat-bridge for nozzle cooling with a flexible Cu strands connection to the coldhead, 4: first set of sextupole magnets, 5: medium field rf transition unit, 6: central support plate, 7: one of two rotational feed-throughs enabling shift of the lower baffle, 8: second set of sextupole magnets, 9: rotating beam chopper, 10: weak and strong field rf transition units, 11: vacuum gate valve between ABS and ANKE target chamber, 12: schematical indication of the storage cell). The labels I to V denote the chambers of the differential pumping system.

the rf transition units, and the slow control system are described in the subsequent subsections.

B. Pumping System

The system of pumps on the chambers I to V of the ABS (Fig. 1) is shown in Fig. 2, the types of the pumps, their pumping speeds, and the achieved pressures are listed in Table I. Chamber I with the highest gas load, due to the effect of the skimmer, is pumped by two strong turbomolecular pumps. Each of them is backed by a smaller turbomolecular pump. Their exhausts are connected to a common pump of the same type. The total compression ratios of the serially connected turbomolecular pumps yields sufficient pumping speed for a primary molecular gas flow up to 3 mbar l/s into the dissociator. The line of pumps is backed by two oil free membrane pumps. According to the lower gas load, chamber II is evacuated by a simpler line consisting of two turbomolecular pumps and a membrane pump. All turbomolecular pumps are operated with use of synthetic oil[20]. Compared to mineral oil, synthetic oil allows longer pumping of hydrogen before oil exchange becomes mandatory. Strong cryopumps are utilized on chambers III and IV, while the lowest chamber with the WFT and SFT units is evacuated by a smaller cryopump. All cryopumps are equipped with temperature-controlled heating units for regeneration on both cooling stages[21]. Heating up to room temperature while pumping the resulting gas load by the bypass system and cooling down again takes about 2.5 to 3 hours.

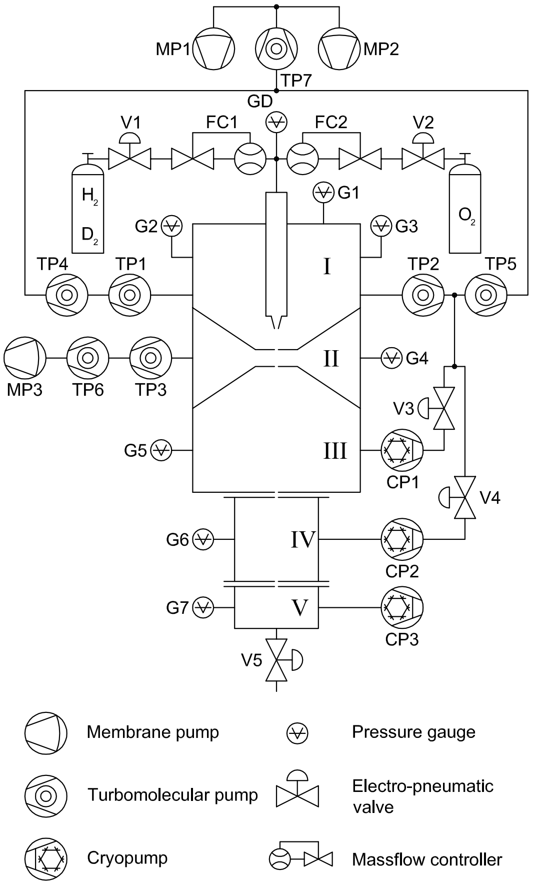

FIG. 2. The system of pumps on the chambers I to V of the ABS (Fig. 1). The specifications of the pumps are listed in Tab. I. The figure also contains the bypass system for the gas load from regeneration of the cryopumps.

C. Baffles

The layout of the baffles had been defined by the necessary narrow vertical extension of the ABS and the requirement to provide sufficient pumping speed in view of the heavy gas load to the vacuum chambers I and II. Furthermore, the construction aimed at the possibility of axial movements from outside to optimize the beam parameters by variation of the distances between nozzle, skimmer, and diaphragm. The resulting shape for the upper baffle is shown in Fig. 3. Except for details in the openings, the lower baffle, carrying the diaphragm, is identical. The layout of the upper vessel and the baffles was done under the boundary conditions that, on the one hand, the baffles have to be movable within the vessel and, on the other hand, the slits between cylindrical surfaces of the baffles and the inner surface of the vessel has to be narrow to reach a small gas conductance. The diameter of the inner vessel surface is 389.2 mm with a longitudinal and non-circular tolerance of +0.2 mm, the outer diameters of both baffels are $(388.7_{-0.2})$ mm. The

TABLE I. List of the devices employed in the ABS pumping system, composed of turbomolecular pumps (TP), membrane pumps (MP), and cryopumps (CP), with nominal the individual capacities C_{H_2}, the pumping speeds S_{H_2}, and the achieved pressures at a primary gas flow of 1.0 mbar l/s.

Chamber	Device	Type	C_{H_2} [bar l]	S_{H_2} [l/s]	Pressure [mbar]
I	TP1-2	TPH 2200[a]		2800	10^{-4}
	TP4-5,7	TMH 260[a]		180	
	MP1-2	MVP 100-3[a]		1.8/1.2[c]	
II	TP3	TPH 2200[a]		2800	10^{-6}
	TP6	TMH 260[a]		180	
	MP3	MVP 100-3[a]		1.8/1.2[c]	
III	CP1	COOLVAC 3000[b]	28[d]	5000	10^{-7}
IV	CP2	COOLVAC 1500[b]	28[d]	5000	$5 \cdot 10^{-8}$
V	CP3	COOLVAC 800[b]	4.3[d]	1000	$5 \cdot 10^{-8}$

[a] Pfeiffer Vacuum GmbH, 35614 Asslar, Germany.
[b] Leybold Vakuum GmbH, 50968 Köln, Germany.
[c] Pumping speed at 1000 mbar/10 mbar
[d] At 10^{-6} mbar.

conductances of the slits of $\leq 5\,l/\mathrm{s}$ are small compared with the applied pumping speed. Because of the complicated shape, identical raw pieces of cast Al[22] were machined to the final dimensions. Contrary to the lower baffle, the upper baffle until now has to be installed together with the flange of the upper vessel at a fixed axial position (cf. Fig. 1). In order to reach full flexibility in varying the nozzle, skimmer, and collimator relative positions from outside, the installation of rotational feedthroughs in the flange of the upper vacuum vessel is necessary, a foreseen but not yet implemented feature.

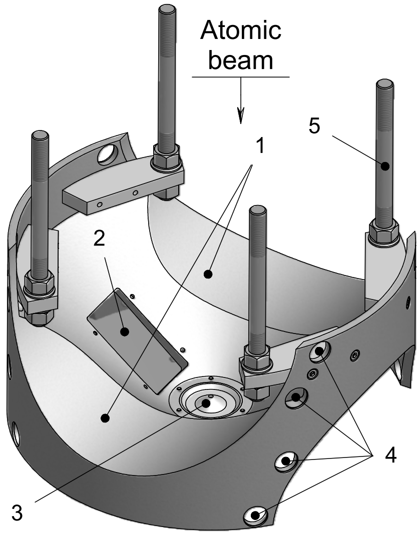

FIG. 3. 3D drawing of the upper baffle, separating the vacuum chambers I and II, with the two wide cuts in front of the turbopumps (1) and the openings for the viewport (2), the skimmer (3), four of the 16 ball bearings (4) and the four supporting rods (5).

D. Dissociator

To dissociate molecular hydrogen or deuterium to neutral atoms, an rf discharge is employed which is fed by a 13.560 MHz generator[23] delivering up to 600 W into a $50\,\Omega$ load. The layout of the dissociator, shown in Fig. 4, is similar to that of the FILTEX design[24,25]. The discharge tube ($\varnothing 11 \times 1.5\,\mathrm{mm}$)[26] is surrounded by two coaxial tubes ($\varnothing 20.4 \times 1.8\,\mathrm{mm}$ and $\varnothing 28 \times 2\,\mathrm{mm}$), all three are made from borosilicate glass[27]. The coolant streams from the inlet connection down between the discharge tube and the middle tube and, after flow reversal at the lower end (Fig. 5, label 2) it streams up in the outer slit to the outlet connection. In a closed loop, the coolant inlet temperature (typically 15 °C for a 50% water – 50% ethanol mixture) is stabilized by a cooling thermostate[28], which would allow coolant temperatures down to −80 °C. The rf coil and the capacitor, at fixed relative positions, can be positioned from outside by means of a sliding rf connection[29] and the feed-through ground connection. This enables variation of the plasma-nozzle distance to optimize the atomic beam intensity while the plasma is burning. The treatment of the discharge tube and the nozzle prior to installation is described in Appendix A.

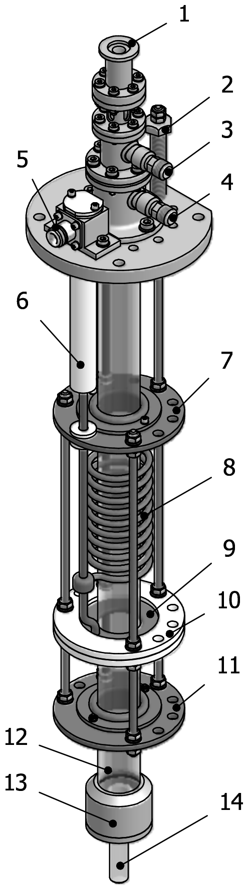

FIG. 4. 3D drawing of the dissociator (1: gas inlet, 2: sliding ground connection, 3: coolant inlet, 4: coolant outlet, 5: rf input, 6: sliding rf connection, 7: grounded capacitor plate, 8: rf coil, 9: rf-fed capacitor plate, 10: isolating plastic support rings, 11: grounded limiter plate, 12: lower end of the coolant-guiding tubes, 13: tube support and connection to the coldhead (details are given in Fig. 5), 14: lower end of the discharge tube).

E. Nozzle

The nozzle, cooled via the heat bridge, and the surrounding components are shown in Fig. 5. The nozzle, made from 99.5% Al, has a simple conical shape with the tip cut. Comparative measurements show that nozzles with sharp edges as used, e.g., in the Madison source[9] do not yield higher atomic beam intensities. First, a sharp edge is more difficult to produce due to the softness of pure Al. Second, the low heat conductance of a sharp edge leads to appreciable temperatures of the nozzle tip, caused by recombination of atoms on the nozzle surface.

The temperature at the bottom of the nozzle is measured with a Pt-100 sensor and it is stabilized with an accuracy of ±0.5 K utilizing a heater. Measurements with temperature sensors placed along the outer nozzle surface have shown a temperature increase from 60 K at the nozzle bottom to ∼200 K at the sharp nozzle tip. In the following, the nozzle temperature is defined as that measured with this Pt-100 sensor.

With the present system of sextupole magnets, the maximum atomic beam intensity feeding the storage cell is obtained with a nozzle-orifice diameter of 2.3 mm and a nozzle-tip to skimmer-tip distance of 15 mm at a skimmer-tip diameter of 4.4 mm and a skimmer-tip to diaphragm distance of 17 mm. The 2 mm thick diaphragm with a conical bore, opening from 9.5 mm to 9.9 mm towards the first permanent sextupole magnet, shields the magnet from heating by atoms recombining on its surface. The slit between the diaphragm and the front face of the magnet enables pumping of gas from the entrance to the magnet.

The Teflon washer and the stainless steel support separate the cold lower end of the heat bridge from the warm lower end of the dissociator. The dimensions of these two components and the sliding heat connector, a worked-over sliding high current connector similar to the rf connector in the dissociator, define the temperature of the lower end of the discharge tube relative to that of the nozzle. The discharge tube, adapted at its lower end to the nozzle by a chamfered edge, is pressed to the nozzle by a viton O-ring at its upper end. The two O-rings around the discharge tube in the lower part of the dissociator seal against the atmosphere. By this design, only minor forces are exerted to the discharge tube.

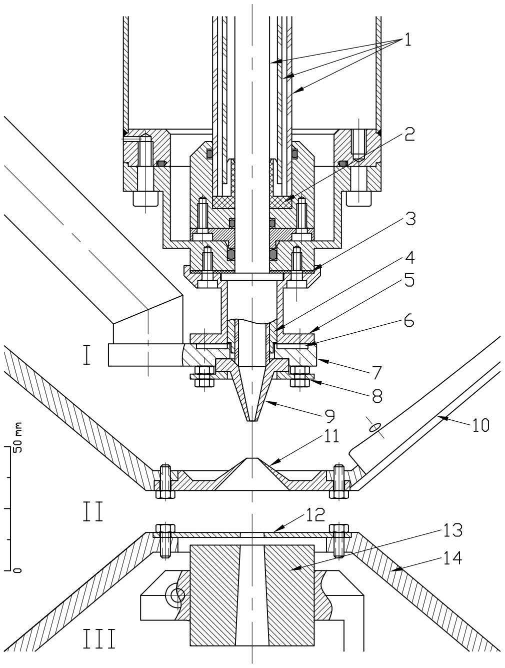

FIG. 5. Technical drawing including the lower end of the heat bridge and the dissociator, the nozzle surroundings, and the first sextupole magnet (in scale, 1: discharge and coolant-guiding tubes, 2: coolant-reversal piece, 3: heat flow reducing Teflon washer, 4: sliding heat connection, 5: stainless steel connector, 6: groove for nozzle-heating element, 7: lower end of the Cu heat bridge, 8: nozzle fixture, 9: nozzle, 10: baffle, separating the chambers I and II, with a viewport, 11: stainless steel beam skimmer, 12: Cu diaphragm, 13: first sextupole magnet, and 14: baffle separating the chambers II and III.

The removable viewport in the baffle and the window flange in the upper vacuum vessel (on the right-hand side of chamber II in Fig. 1) allows one to observe the nozzle status from the outside and to exchange nozzles without removal of the dissociator from the setup.

The heat bridge from the coldhead to the nozzle is made from electrolytic Cu. The flexible link between the coldhead and the heat bridge, consisting of about 200 high-purity Cu strands of 1 mm diameter, allows for the thermal expansions of the cold and the warm components. The total cross section of the strands and their heat conductance is smaller than that of a massive Cu body. This deficiency, however, is reduced by clamping the flexible link directly to the coldhead. At its operating temperature of about 30 K, the thermal conductivity of Cu is about 11, 9, and 5 times higher than that at 300, 100, and 60 K, respectively[30]. Thus, the reduction of the conductance of the entire heat bridge by the flexible link is minimized by placing it at the coldhead. With the present system, cooling the nozzle down from room temperature to 60 K needs about 1.5 hours. The heating element facilitates warming up to room temperature within about one hour.

Furthermore, avoiding the maze of cold Cu strands around the nozzle, i.e., a labyrinthic cold surface, compared to an earlier solution[31] leads to improved pumping conditions in the nozzle-skimmer area, where the highest gas load has to be pumped off.

In an earlier phase of the ABS development, attempts have been made to use a cryogenic Ne heat-pipe of 20 W cooling power instead of the usual solid Cu bridge to achieve faster cooling and warming of the nozzle because of the lower heat capacity[32]. An observed instability in the necessary operation mode, however, lead to difficulties in nozzle-temperature stabilization. In view of the fact that the cooling and warming-up times, reached with the Cu bridge, were satisfying and that its use avoids the additional precautions, imposed by the heat-pipe operation, it has been replaced by the Cu bridge.

F. Magnet System

The design of the magnet system was made for a set of sextupole magnets consisting of permanently magnetized segments made from NdFeB compounds, delivering pole-tip fields around 1.5 T. Tracking calculations from the nozzle to the feeding tube of the storage cell were performed with the use of a computer code originally developed for the FILTEX ABS[24]. The boundary conditions by the layout of the target setup were the available distance of about 1250 mm from the nozzle to the feeding-tube entrance of 10 mm diameter and the distance from the exit of the last magnet to the feeding-tube entrance of 300 mm, necessary to install the SFT and WFT units and the gate valve between the ABS and the target chamber.

The laboratory velocity distribution of the atoms in the supersonic beam from the nozzle is described by a modified Maxwellian distribution

$$\mathcal{F}(\vec{v}_{\rm d}, T_{\rm b}) = \left(\frac{m}{2\,k\,T_{\rm b}}\right)^{3/2} \exp\left[\frac{-m}{2\,k\,T_{\rm b}}(\vec{v}-\vec{v}_{\rm d})^2\right], \quad (1)$$

where m is the mass of the atoms and k is the Boltzmann constant. According to time-of-flight studies[33], the drift velocity along the beam axis, $v_{\rm d}$, and the beam temperature $T_{\rm b}$ for a primary molecular gas flow of 1 mbar l/s and a nozzle-orifice diameter of 2 mm follow a linear dependence on the nozzle temperature $T_{\rm n}$. For hydrogen $v_{\rm d}[\rm m/s] = 1351 + 6.1 \cdot T_{\rm n}[\rm K]$ and $T_{\rm b} = 0.29 \cdot T_{\rm n}$ and for deuterium $v_{\rm d}[\rm m/s] = 1070 + 3.45 \cdot T_{\rm n}[\rm K]$ and $T_{\rm b} = 0.25 \cdot T_{\rm n}$.

As starting conditions of a track a random generator selects a point in the nozzle orifice, one within the diaphragm in front of the first magnet, and an atom velocity $|v|$. In linear molecular flow approximation (cf. the discussion in Ref.[34]) this defines $\vec{v}$ for the track between the nozzle and the first magnet. According to the geometrical boundary conditions and the velocity distribution of Eq. (1) the event is either rejected or used in the further track calculation. Within the magnet the evolution of the track is calculated stepwise by numerical integration of the equation of motion over integration times of $2\,\mu s$, corresponding to track lengths of 3.6 mm for a typical particle velocity of 1800 m/s. The pure radial force, acting on an atom within the field of the sextupole magnet, is $\vec{F}_{\rm r} = -\mu_{\rm eff} \cdot \delta B/\delta r \cdot \vec{r}/r$. The effective magnetic moment, resulting from the Breit-Rabi diagram (e.g., Ref.[35]) as $\mu_{\rm eff} = \delta W/\delta B$, is positive (negative) for atoms in the hyperfine states with the electron spin parallel (antiparallel) to $\vec{B}$ in the magnet aperture which therefore are deflected towards (away from) the beam axis. In the drift sections between the two magnet groups and between the last magnet and the feeding tube the trajectories are assumed as straight lines.

A variety of systems were studied, all under the assumption of $T_{\rm n} = 60\,\rm K$ and pole-tip fields of 1.5 T. A system utilizing 6 magnets was found to yield satisfying both separation of the atoms in the $\mu_{\rm eff} < 0$ and $\mu_{\rm eff} > 0$ states and focusing of the $\mu_{\rm eff} > 0$ states into the feeding tube. Optimization of the parameters led to the system listed in Table II. (The tracking calculations, yielding the magnet dimensions for the order to the manufacturer had been performed for a slightly different geometry.) The table gives the two distances, at which intensity measurements with the compression tube were performed. The Fig. 6 shows the projection of the trajectories of H atoms in the $\mu_{\rm eff} > 0$ states, calculated for this system.

TABLE II. Final dimensions and axial positions of the source components (pole-tip field strenghts B_0^* as measured after delivery[36], inner diameters ($\varnothing_0$), outer diameters ($\varnothing_1$), axial dimensions (ℓ), and distances (Δ) between the components. The lower three lines give the two distances and the dimensions of the compression tube used in the intensity measurements.

component	B_0^* [T]	$\varnothing_0$ [mm]	$\varnothing_1$ [mm]	ℓ [mm]	Δ [mm]
Nozzle orifice		2.3	3.3		
					15.0
Skimmer		4.4/30.4[a]		13.0	
					16.9
Diaphragm		9.5/9.9[a]		2.0	
					3.6
Magnet #1	1.630	10.40/14.12[a]	39.98	40.01	
					9.4
Magnet #2	1.689	15.98/22.12[a]	64.04	65.01	
					9.4
Magnet #3	1.628	28.04	94.00	70.01	
					429.7
Magnet #4	1.583	30.04	94.02	38.01	
					101.0
Magnet #5	1.607	30.06	94.00	55.01	
					15.0
Magnet #6	1.611	30.02	94.04	55.00	
					300.0
					337.0
Compr. tube		10.0	11.0	100.0	

[a] Conical opening,the first number denotes the measured diameter of the entrance, the second that of the exit aperture.

One recognizes two groups of trajectories, one with an intermediate focus and another one with focusing into the feeding tube. The present result like those of other groups (see e.g., Ref.[33]) confirms the expectation[37] that the transmission as function of the atom velocity should show two maxima, one below and one above the most probable velocity.

The transmission Tr of the system is defined as the fraction of tracks, ending within the entrance of the feeding tube, to those passing the diaphragm in front of the first sextupole magnet. For the four hyperfine states of hydrogen[38], the calculations yield $Tr(|1\rangle) \sim Tr(|2\rangle) = 0.42$ (for both $\mu_{\rm eff} > 0$), and $Tr(|3\rangle) = 0.001$, and $Tr(|4\rangle) = 0.0004$ (for both $\mu_{\rm eff} < 0$).

The performed tracking calculations do not account for intra-beam and residual-gas scattering. The calculated transmissions thus only allowed one to estimate upper limits of the expected atomic beam intensity $I_{\rm in}$ into the feeding tube. For a primary molecular flow $q(\rm H_2)$, the intensity $I_{\rm in}(\rm H)$ with atoms mainly in the states $|1\rangle$ and $|2\rangle$ ($\mu_{\rm eff} > 0$) was expected as

$$I_{in}({\rm H}) = q({\rm H_2}) \cdot 2\alpha \cdot \frac{\Omega}{2\pi} \cdot \frac{1}{4} \sum_{i=1}^{i=4} Tr(|i\rangle). \quad (2)$$

For the degree of dissociation α a routine value of 0.8 (see e.g., Ref.[9]) was assumed. $\Omega = 0.022\pi$ is the solid angle covered by the collimator aperture. The factor 1/4 reflects the assumption that the four substates in the atomic beam from the nozzle are equally populated. For $q(\mathrm{H_2}) = 1\,\mathrm{mbar}\,l/\mathrm{s}$ or $2.7{\cdot}10^{19}\mathrm{H_2}$ molecules/s one expects $I_{in}(\mathrm{H}) \sim 1 \cdot 10^{17}$ H atoms/s.

As described in the subsequent section, the rf transition units are used to change the relative occupation numbers of the states. The trajectory code allows one to simulate this change by assigning a $\mu_{\rm eff}$ of one of the states to the atoms before they pass a magnet. As an example, the medium-field transition unit (MFT) behind magnet No. 3 (see Fig. 1) brings H atoms from state $|2\rangle$ into state $|3\rangle$. This is simulated by assigning $\mu_{\rm eff}(|2\rangle) > 0$ to the atoms in the magnets $1-3$ and $\mu_{\rm eff}(|3\rangle) < 0$ in the magnets $4-6$, where they get deflected from the beam axis. This results in a small value $Tr(|2\rangle) = 0.017$. From this value and the above value $Tr(|1\rangle) = 0.42$ the vector polarization is expected as

$$p_z = \frac{Tr(|1\rangle) - Tr(|2\rangle)}{Tr(|1\rangle) + Tr(|2\rangle)} = 0.91 \qquad (3)$$

under the assumption of 100 % efficiency of the transition unit.

The design and the properties of the permanent sextupole magnets[39] were discussed in an earlier paper[36]. To achieve the pole-tip field values of ~1.5 T, each magnet was produced from 24 segments employing three different types of NdFeB compounds. The expected pole-tip values (Table II) and the precise radial dependence $B(r) \sim r^2$ within the magnet apertures were confirmed. For the first time the predicted high multipole components[40] up to a 102-pole structure very near to the aperture surface could be measured[36].

After the field measurements, the magnets were encapsulated to prevent diffusion of hydrogen into the magnet material, which might deteriorate the magnetic properties, and to avoid the pumping of gas from the sintered magnet bodies. The housings were made from thin stainless steel cans of 0.2 mm thickness for the conical and cylindrical walls within the magnet apertures and 0.3 mm for the front and end covers. During the final welding to close the housings with magnets installed, the local temperature of the magnet material had to be kept below the Curie temperature of 60 °C. This was achieved by welding with the use of a pulsed 15 Hz Nd:YAG laser, delivering 1.1 J in a pulse of 2 ms[41]. Overlapping weld spots of ~0.3 mm diameter, set around the adjacent circular, 0.2 mm thick weld lips, allowed one to finish the housings with leak rates $\sim 10^{-10}\,\mathrm{mbar}\,l/\mathrm{s}$. Inside the housings the magnets were fixed to suppress axial and rotational movements caused by the force of the adjacent magnets. Finally the free slits within the housings were filled by ~20 mbar krypton to enable leak tests by mass spectroscopy.

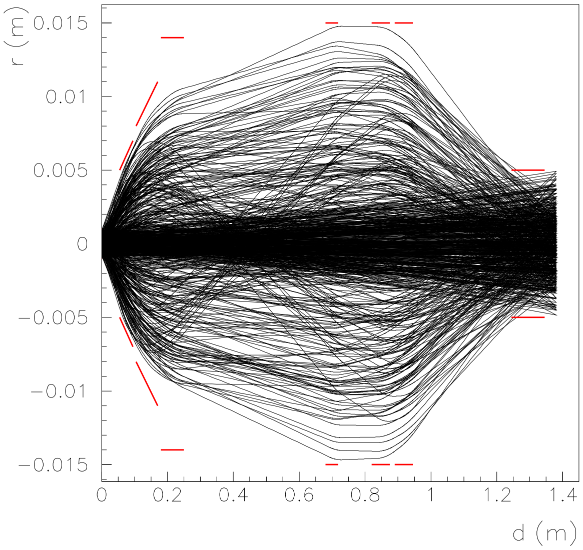

FIG. 6. Projection of the 3-dimensional trajectories of hydrogen atoms in hyperfine states $|1\rangle$ and $|2\rangle$ (effective magnetic moment $\mu_{\rm eff} > 0$)) from the nozzle ($\varnothing = 2\,\mathrm{mm}, T_{\rm n} = 60\,\mathrm{K}$) to the storage cell calculated for the magnet arrangement of Table II and pole-tip fields of 1.5 T. The positions and lateral dimensions of the six magnets and the feeding tube are indicated (in red).

G. Radio Frequency Transition Units

The ABS is equipped with three types of transition units, a weak field, a medium field, and a strong field rf transition unit (WFT, MFT, and SFT units). Together with the selecting properties of the sextupole magnets, they enable one to achieve all vector and tensor polarizations of the atomic hydrogen and deuterium gas in the storage cell. In all three units, transitions between the hyperfine states, split according to the Breit-Rabi diagram by a static magnetic field (see e.g., Ref.[35]), are induced by the magnetic component ($B_{\rm rf}$) of an rf field, leading to changes in the population of the states. The static field $B_{\rm stat}$ consists of two parallel components, a homogeneous field $B_{\rm hom}$ and a superimposed weaker gradient field $B_{\rm grad}$, both orthogonal to the beam direction. The field gradient along the beam direction is required to satisfy the condition of adiabatic passage[35,42].

The assemblies of the WFT and the MFT units are similar[43]. The layouts follow those of the units developed for the HERMES experiment[44]. In both units the rf field is produced by a coil with the axis along the beam direction, and consequently $B_{\rm rf}$ orthogonal to $B_{\rm stat}$. The MFT unit is shown in Fig. 7. Figure 8 schematically shows one of the grooved aluminum frames with the windings producing the gradient field. A WFT unit is operated in a weak magnetic field, $B_{\rm stat} \leq 10$ G for hydrogen and ≤ 5 G for deuterium, where the total atomic spin F is a good quantum number. In hydrogen the

$F = 1$ levels $|1\rangle$, $|2\rangle$, and $|3\rangle$ with magnetic quantum numbers $m_\mathrm{F} = +1$, 0, and -1, respectively, can be regarded as equally spaced. In deuterium the same holds for the four $F = 3/2$ levels $|1\rangle$, $|2\rangle$, $|3\rangle$, and $|4\rangle$) with $m_\mathrm{F} = +3/2, +1/2, -1/2$, and $-3/2$, respectively, and for the two $F = 1/2$ levels $|5\rangle$ and $|6\rangle$ with $m_\mathrm{F} = -1/2$ and $+1/2$, respectively. The magnetic component of the rf dipole field induces transitions between each pair of neighboring m_F states with $\Delta m_\mathrm{F} = \pm 1$. $|\Delta m_\mathrm{F}| = 2$ transitions are forbidden. The interchange of the population between the states $|1\rangle$ and $|3\rangle$ in hydrogen, e.g., is caused by a two-quantum transition via the intermediate state $|2\rangle$. In the classical description of the adiabatic passage method[42] the population change should not depend on the sign of the magnetic field gradient relative to the beam direction. An exact quantum-mechanical treatment[45,46], however, indicates that cleaner population changes from state $|1\rangle$ to $|3\rangle$ in hydrogen and from state $|1\rangle$ to $|4\rangle$ in deuterium are obtained with a negative field gradient, i.e., a B_rf field decreasing in the beam direction. Deviations from adiabaticity are discussed in Ref.[45,47].

The MFT unit is operated at higher values of B_stat, where the differences in the energy spacings of pairs of hyperfine states with $\Delta m_\mathrm{F} = \pm 1$ allow one to select single transitions. Originally developed for an polarized alkali ion source[48], the MFT unit now is a standard component in polarized hydrogen and deuterium sources as discussed, e.g., in Ref.[49]. Appropriate choice of B_hom, B_grad, and the rf frequency allows one to induce selected transitions $|1\rangle \leftrightarrow |2\rangle$ and $|2\rangle \leftrightarrow |3\rangle$ in hydrogen or $|1\rangle \leftrightarrow |2\rangle$, $|2\rangle \leftrightarrow |3\rangle$, and $|3\rangle \leftrightarrow |4\rangle$ in deuterium. Furthermore, the choice of the field gradient allows one to achieve consecutive transitions. As an example a negative field gradient in the MFT unit behind the first set of magnets, i.e., a B field decreasing in beam direction, at a fixed rf frequency leads to the sequence of the transitions $|3\rangle \rightarrow |4\rangle$, $|2\rangle \rightarrow |3\rangle$, and finally $|1\rangle \rightarrow |2\rangle$ in deuterium, leaving the state $|1\rangle$ empty.

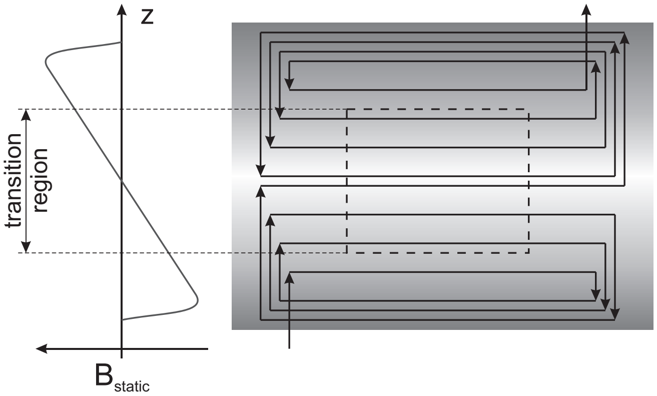

FIG. 8. Arrangement of the windings producing the static gradient field B_grad shown in the left-hand side of the figure. In all transition units the field lies in the direction of the static homogeneous field, the field gradient dB/dz lies in the beam direction which defines the z axis. In z direction, the transition reagion (indicated by the dashed lines) is confined to the range of constant gradient by the Al tubes, in orthogonal direction by the beam diameter.

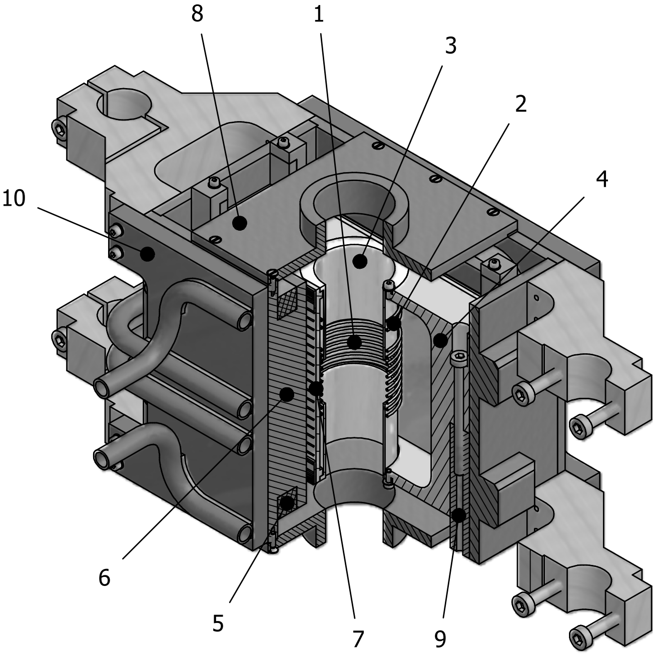

FIG. 7. Three-quarter-section view of the MFT unit with the support structure (1: self-supporting rf coil with spacers, 2: pick-up loop, 3: Al tubes defining the length of the transition-inducing rf field, 4: Cu cavity, 5: coil around the pole shoe (6), providing the static field B_stat, 7: slit between pole shoe and cavity wall housing the gradient-field coil, 8: components of the static magnet yoke, also serving as shielding against external fields, 9: cavity-positioning element, 10: Cu pads cooled by means of water-carrying tubes. The cavity with the rf coil and the pick-up loop can be taken out from the surrounding components.

The SFT unit is used to induce transitions between states in the upper and lower hyperfine multiplet in hydrogen and deuterium. Contrary to the historical name, indicating a strong magnetic field, the SFT unit is operated with magnetic fields comparable to those used in the MFT unit. The transition frequencies are comparable with those of the hyperfine splitting (1420 MHz for hydrogen and 327 MHz for deuterium), and thus are much higher than those in the WFT and MFT units. The rf field in a SFT unit is produced by a twin-line resonator inside a Cu box tuned to the $\lambda/4$ resonance[50]. The SFT unit[51] is shown in Fig. 9. Again, the layout follows that of the unit used in the HERMES experiment[44]. Two variable capacitors at the free ends of the conducting rods, fed by the rf power with a relative phase shift of 180 °, allow one to tune the device.

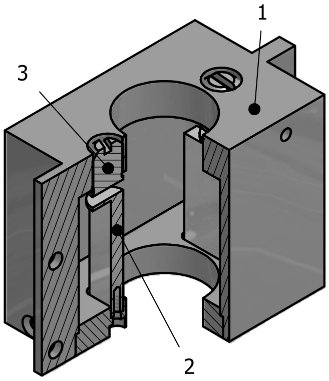

FIG. 9. Three-quarter-section view of the rf cavity of the SFT unit for deuterium (1: the two resonant-field creating conductors, 2: the adjustible capacitor plates, 3: Cu cavity). The inner dimensions of the cavity are 56 mm along B_{stat}, 36 mm orthogonal to it and 36 mm height. The cross section of the conductors is $14 \times 4\,\text{mm}^2$.

H. Slow Control System

Industrial components, providing reliable and long-term support, were selected for the control system of the whole setup consisting of the ABS and the diagnostics tools, the storage cell positioning system, the Lamb-shift polarimeter, and the supply system of a calibrated flow of unpolarized molecular gas. The interlock system has been implemented on the basis of SIEMENS SIMATIC S7-300 family of programmable logic controllers. In order to unify the interfacing to the control computer, all front-end equipment is connected via the PROFIBUS DP field-bus. The process control software was implemented using the Windows-based WinCC toolkit from SIEMENS. The system controls the operation of the pumps and the valves. It reads the pressure gauges and controls the regeneration cycles of the cryopumps. Via a control network, the temperature of the nozzle is stabilized within ±0.5 K. Furthermore, all power-supply units, rf generators and amplifiers are set and controlled. The whole variety of components to be controlled, the logical structure of the control and interlock system, and a separate device for parameter studies are described in Ref.[52].

III. STUDIES OF THE FREE HYDROGEN JET

A. Atomic beam profile near the nozzle

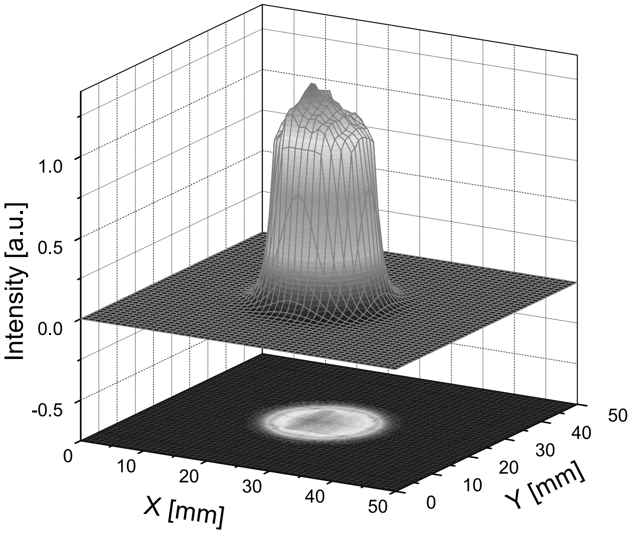

FIG. 10. Two-dimensional profile of the atomic hydrogen beam 10 mm from the nozzle, deduced from recombination heating of gold-plated tungsten wires of 5 μm in a 8×8 wire grid.

A novel device has been used to measure the profile of an atomic beam via the deposition of recombination heat on thin wires in a two-dimensional grid[53,54]. Atoms stuck on the surface of gold-plated tungsten wires of 5 μm diameter recombine and are reemitted as molecules. The recombination heat (4.476 eV per hydrogen molecule) leads to a change of temperature and, thus, resistance along each wire. The measurement of the resistance changes of all the wires in the grid allows one to deduce the center and the profile of the beam. Figure 10 shows the beam profile resulting with a 8×8 wire grid positioned between skimmer and collimator, performed as a first proof of the method. Later, such a device has been used to compare measured and calculated beam profiles along the beam axis between nozzle and skimmer[34].

B. Degree of dissociation of the free atomic jet

The dissociation of the primary molecules is achieved by the interaction of the electrons and the hydrogen or deuterium molecules in the plasma of the dissociator. The degree of dissociation of the beam from the nozzle depends on the rf power, applied to maintain the plasma, the primary molecular gas flow into the dissociator, and the temperature of the nozzle and the lower end of the discharge tube. These dependencies have been studied before installation of the sextupole magnets with a setup containing a crossed-beam quadrupole mass spectrometer[55,56].

$$\alpha = \frac{\rho_{\text{a}}}{\rho_{\text{a}} + 2 \cdot \rho_{\text{m}}}, \tag{4}$$

The admixture of molecules in an atomic beam is described by the degree of dissociation, where ρ_{a} and ρ_{m} are the densities of atomic and molecular hydrogen or deuterium in the beam. Other authors (e.g., Ref.[13]) use the atomic and molecular intensities I_{a} and I_{m} in the definition of the degree of dissociation (α_{I}) in Eq. (4). The two definitions of are related by

$$\frac{I_{\text{m}}}{I_{\text{a}}} = \frac{\bar{v}_{\text{m}}}{\bar{v}_{\text{a}}} \cdot \frac{1-\alpha}{2\alpha} = \frac{1-\alpha_{\text{I}}}{2\alpha_{\text{I}}}\,. \tag{5}$$

This quantity was determined with the quadrupole mass spectrometer (QMS) in a conventional way as

$$\alpha = \frac{S_\mathrm{a}^*}{S_\mathrm{a}^* + 2\, k_v\, k_\mathrm{ion}\, k_{det} S_\mathrm{m}}. \tag{6}$$

Here, $S_\mathrm{a}^* = S_\mathrm{a} - \delta S_\mathrm{m}$ denotes the atomic signal, corrected for dissociative ionization. The parameter $\delta = 0.0141$ was obtained following the method described in Ref.[31]. The coefficient $k_v = \overline{v}_m/\overline{v}_a$, accounting for the difference in atom and molecule velocity, was chosen as $1/\sqrt{2}$ under the assumption of thermalization of the beam emerging from the nozzle. Furthermore, $k_\mathrm{ion} = 0.64$ [57] accounts for the differences in ionization cross section for atomic and molecular hydrogen, and $k_\mathrm{det} = 0.84$ for the detection probability[55]. As an example of the parameter studies, Fig. 11 shows the deduced dependencies on the rf power for a set of primary molecular hydrogen gas flows. For typical flow values $q(\mathrm{H}_2) \leq 1.0\,\mathrm{mbar}\; l/s$ a saturation value around 0.8 was obtained.

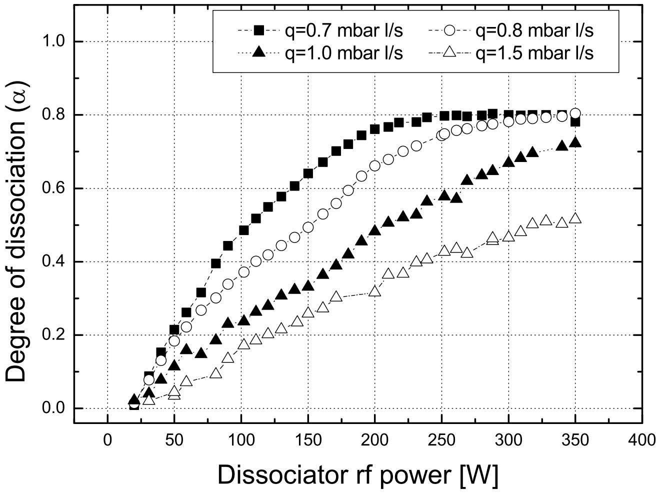

FIG. 11. Degree of dissociation α of the free hydrogen jet as function of the applied rf power for different primary molecular hydrogen flows and a nozzle temperature of 70 K.

IV. BEAM INTENSITY

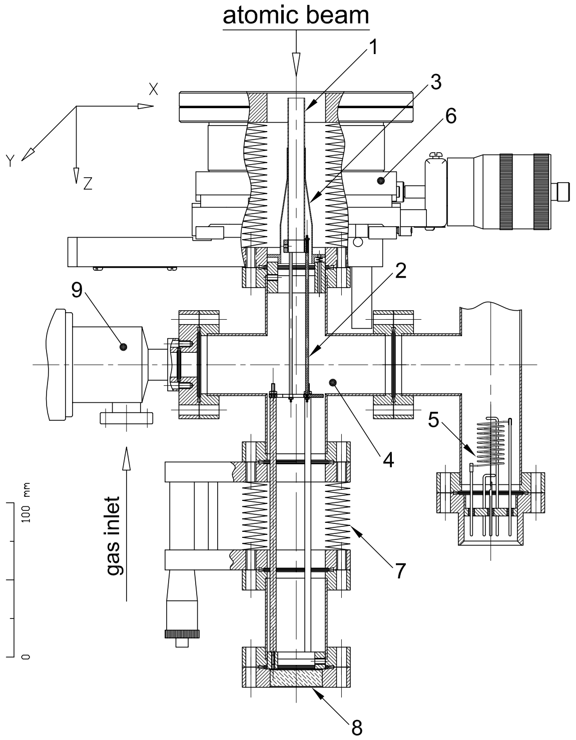

FIG. 12. Side view of the compression-tube setup, made from standard ultra-high-vacuum components, with a partial cut along the axis. (1: compression tube, 2: support of the compression tube based on the lower flange, 3: narrow tube around 1 closing the upper volume and allowing axial shifts of the tube by the support, 4: compression volume, 5: hot-cathode pressure gauge, 6: xy manipulator, 7: z manipulator, 8: glass viewport, 9: electromagnetic valve for gas inlet.

The intensity of the polarized beam from the ABS together with the layout of the storage cell determines the areal density of the target gas. The intensity of the beam has been measured with the use of a compression-tube setup[58,59], shown in Fig. 12, to optimize the ABS operation parameters. The measurements were performed at a 300 mm distance from the compression-tube entrance to the last magnet and an inner tube diameter of 10.0 mm as set in the tracking calculations. The length of the compression tube of 100 mm was made equal to that of the foreseen feeding tube of the storage cell. The narrow tube around the compression tube on a support, based on the lower flange, separates the volume around the tube from the compression volume. The xy manipulator serves for centering the tubes and for intensity-profile measurements. The construction allows axial shifts of the compression tube by the z manipulator and the use of tubes of different diameters.

The intensity of the beam, entering the compression volume through the compression tube, is measured via the pressure in the compression volume. It is determined by the equilibrium between the incoming beam intensity I_in and the outgoing intensity I_out. Under the assumption of a pure atomic beam and complete recombination in the compression volume

$$\begin{aligned} I_\mathrm{in}(\mathrm{atoms/s}) &= 2 \cdot I_\mathrm{out}(\mathrm{molecules/s}) \\ &= 2 \cdot \Delta P \cdot C_\mathrm{tube} \\ &= 2 \cdot \Delta P \cdot 1.03 \cdot 10^{20} \cdot \frac{d^3}{l}\sqrt{\frac{T}{M}}\ . \end{aligned} \tag{7}$$

Here ΔP is the difference between the pressure measured in the compreesion volume and that in the ABS chamber V. The conductance of the compression tube, C_tube, is determined by the inner diameter d of the tube, its length l, the gas temperature T, and the molar mass M of the gas (given in cm and K, respectively)[60]. The

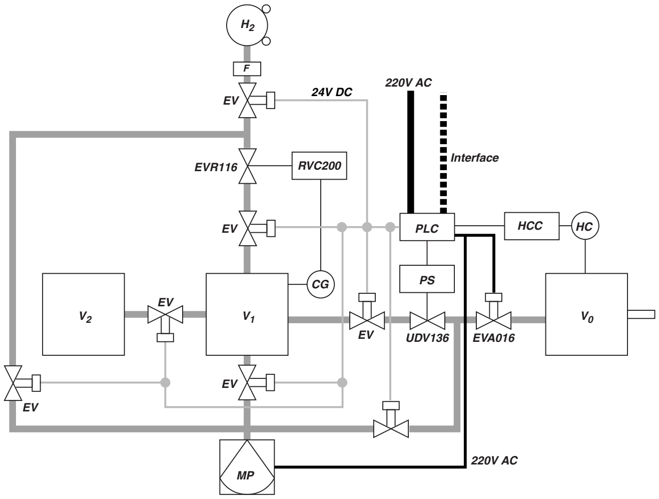

FIG. 13. Source of calibrated molecular gas flow (V_0: compression chamber, V_1: gas-storage chamber feeding V_0 via the needle valve UDV136[a], V_2: chamber of calibrated volume used to determine that of V_1). The pressure in V_1 is measured by the capacitance gauge CG and is kept constant by the dosing valve EVR116 with the gauge controller RVC200. The whole setup, including the evacuation elements can be operated manually or by the programmable logic controller PLC either within the ABS control system[52] or as a separate system.

[a] All the valves and the gauge controller are supplied by Pfeiffer Vacuum GmbH, D–35614 Asslar, Germany (manufacturer Balzers AG, Liechtenstein).

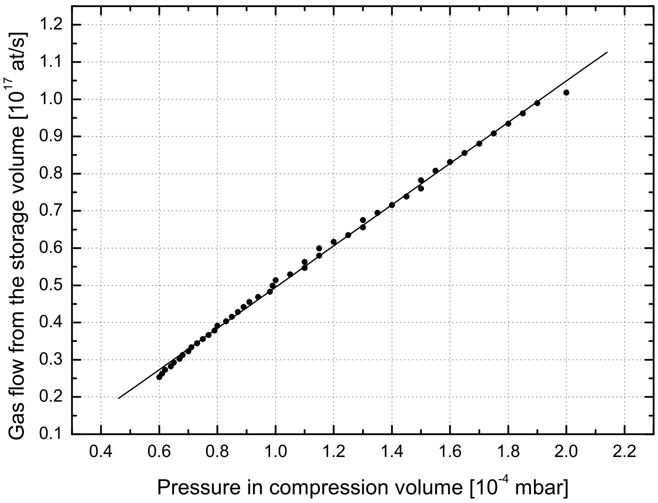

FIG. 14. Calibration curve for hydrogen used to deduce from the measured pressures the intensities of the hydrogen and deuterium beam injected into the compression tube.

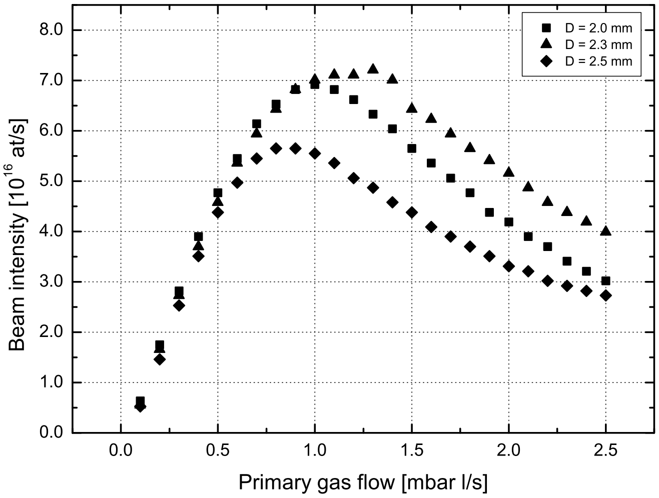

FIG. 15. Intensity of the hydrogen beam (states $|1\rangle$ and $|2\rangle$) injected into the compression tube as function of the primary molecular gas flow for different nozzle diameters D (nozzle temperature 60 K, dissociator power 300 W).

factor 2 takes into account that the same pressure is measured in the hot-cathode gauge for $2 \cdot I_{\mathrm{in}}$ (H atoms/s) and $1 \cdot I_{\mathrm{in}}$ (H_2 molecules/s). For $d = 10\,\mathrm{mm}$, $l = 100\,\mathrm{mm}$, $T = 290\,\mathrm{K}$, and $M = 2$ for hydrogen pressure differences ΔP on the order of 10^{-4} mbar are expected for atomic hydrogen beam intensities in the order of 10^{17} atoms/s. The relation between I_{in} and ΔP for hydrogen has been determined experimentally with the use of a source of calibrated molecular hydrogen gas flow[58,59], depicted in Fig. 13. The measured dependence with a linear fit is shown in Fig. 14. The calibration curve allows one to determine absolute values of I_{in} of hydrogen and deuterium beams. The calibration for deuterium was deduced from the one for hydrogen by scaling with a factor $1/\sqrt{2}$, according to Eq. (7).

The dependences of I_{in} on the dissociator-operation parameters primary molecular hydrogen flow $q(H_2)$, nozzle temperature T_{n}, and dissociator power P_{diss} have been studied to find the optimum values. They are shown in the Figs. 15, 16, and 17, respectively, for different nozzle-orifice diameters. The figures show that for the hydrogen beam (states $|1\rangle$ and $|2\rangle$) with the standard operation parameters $q_{H_2} = 1.1$ mbar l/s, $T_{\mathrm{n}} = 70\,\mathrm{K}$, $P_{\mathrm{diss}} = 350\,\mathrm{W}$, and with a nozzle-orifice diameter of 2.3 mm an intensity of $I_{\mathrm{in}}(\mathrm{H}) = (7.5 \pm 0.2) \cdot 10^{16}$ particles/s is achieved, quite close to the earlier estimate from Eq. (2). Besides the dominant atomic component of H atoms, this value includes small admixtures of H atoms in state $|3\rangle$ and molecular hydrogen. The first kind can be estimated with the use of the calculated transmissions (Sec. II F) as $0.017/0.84 \approx 2\%$. The amount of the second admixture has been measured as described below.

For the deuterium beam (states $|1\rangle$, $|2\rangle$, and $|3\rangle$) the optimization procedure gave an intensity of $I_{\mathrm{in}}(\mathrm{D}) = (3.9 \pm 0.2) \cdot 10^{16}$ particles/s, achieved with $q(D_2) = 0.9$ mbar l/s, $T_{\mathrm{n}} = 65\,\mathrm{K}$, and $P_{\mathrm{diss}} = 300\,\mathrm{W}$, slightly lower than those for hydrogen.

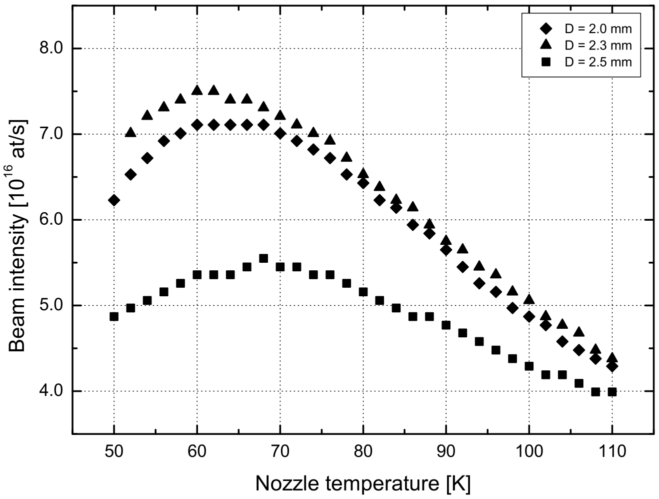

FIG. 16. Intensity of the hydrogen beam (states $|1\rangle$ and $|2\rangle$) injected into the compression tube as function of the nozzle temperature for different nozzle diameters D (primary molecular gas flow 1 mbar l/s, dissociator power 300 W).

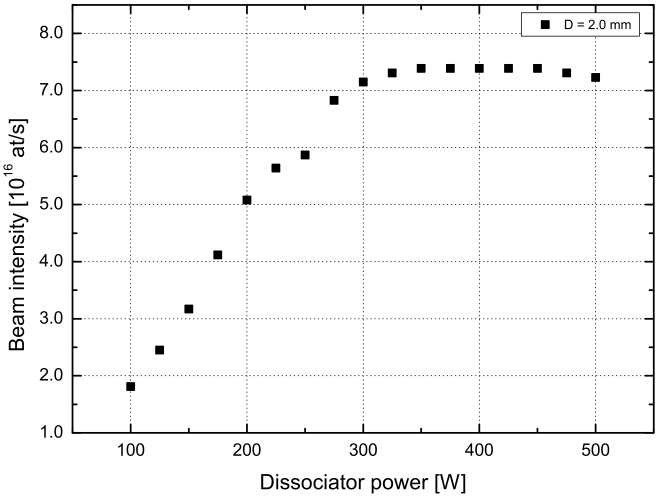

FIG. 17. Intensity of the hydrogen beam (states $|1\rangle$ and $|2\rangle$) into the compression tube as function of the dissociator power for a nozzle diameter of 2 mm (nozzle temperature 60 K, primary molecular gas flow 1 mbar l/s).

V. HYDROGEN BEAM PROFILES

Beam profiles were measured at various positions at various positions behind the last sextupole magnet with the use of

- a compression tube of reduced dimensions (5 mm diameter)
- a crossed-beam quadrupole mass spectrometer, and
- a supplementary method of reduction of MoO_3 by hydrogen.

A. Measurements with the compression tube

For the determination of the beam dimensions at two positions, 300 mm and 337 mm behind the last magnet, the compression tube setup (Fig. 12) was used, making use of the possibility of axial movement by the z manipulator and of that to install a narrower and shorter compression tube of 5 mm diameter and 50 mm length to enhance the spatial resolution. The xy manipulator provided a lateral displacement of the compression tube by ±10 mm in x and y direction. The center coordinates of the geometrical axis of the source had been determined with the use of a bi-directional laser, centered inside the bore of the central support plate (see Fig. 1). The relative intensity distributions in the xz and yz planes, given by the measured pressure in the compression volume, are shown in Fig. 18. Fits by Gaussian distributions to the data yield full widths at half maximum $\Gamma_x = (6.42 \pm 0.09)$ mm, $\Gamma_y = (6.99 \pm 0.06)$ mm for the distributions measured at $z = 300$ mm and $\Gamma_x = (6.27 \pm 0.08)$ mm, $\Gamma_y = (6.58 \pm 0.08)$ mm at 337 mm.

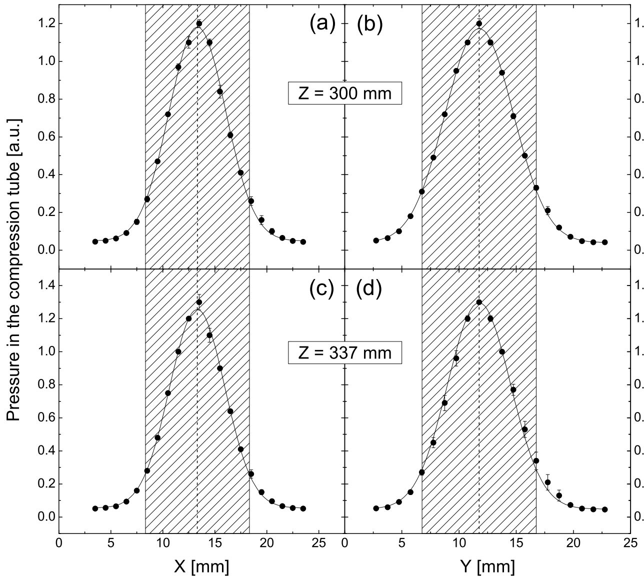

FIG. 18. Cross sections of the beam profile in the mid-plane, measured with compression tube of 5 mm diameter and 50 mm length. Measurements in the xz-plane (a, c) and yz-plane (b, d) performed at two different positions: $z = 300$ mm (a, b) and $z = 337$ mm (c, d) behind the last sextupole magnet of the ABS. The shaded area represents position and dimensions of the compression tube used in intensity measurements.

The center of gravity of the measured profile, defined as

$$r_c = \frac{\sum\limits_{i,j} \sqrt{x_i^2 + y_j^2} \cdot P(x_i, y_j)}{\sum\limits_{i,j} P(x_i, y_j)}, \tag{8}$$

where x_i and y_j give the position of the compression-tube axis and $P(x_i, y_j)$ is the pressure measured in the compression volume. The resulting r_c shows a deviation of 0.12 mm from the geometrical axis of the source. Furthermore, the data measured with the narrow compression tube of 2.5 mm radius can be used to derive the fraction of the beam entering the compression tube of 5 mm radius used in the intensity measurement of Sec. IV. The ratio

$$\eta = \frac{\sum\limits_{0}^{r_i \leq 2.5\ \mathrm{mm}} P(x_i, y_j)}{\sum\limits_{0}^{r_i \leq 10\ \mathrm{mm}} P(x_i, y_j)}, \tag{9}$$

where r_i is the distance of the compression-tube axis to the beam axis, yields $\eta \approx 0.7$.

B. Measurements with the QMS

The beam-profile studies of Sec. V A were extended with a setup utilizing a crossed-beam quadrupole mass spectrometer (QMS) in the setup of Fig. 19. Contrary to the measurements with the compression tube, those with the QMS allow to separate the atomic and molecular fractions in the beam. A 2 mm diameter aperture was installed at the entrance of the sensitive volume of the QMS to improve the resolution compared with that achieved by the compression tube of 5 mm diameter used in measurements of the preceding section. The layout of the setup, presented in Fig. 19, shows that in the present case the profile could not be measured at a distance of $z = 300$ mm to the last magnet. Instead, measurements were performed at $z = 567$ mm and, with installation of an extension tube, at $z = 697$ mm. The xy manipulator enabled displacements of the aperture axis from the geometrical axis of the source in any direction within limits set by the bore diameter of the xy manipulator.

The first measured distribution of the atomic hydrogen (Fig. 20) showed a distinct deviation from azimuthal symmetry, indicating an insufficient relative alignment of nozzle and skimmer. The three threaded rods, supporting the dissociator with the nozzle via the three-legged plate (label 2 in Fig. 1), allow one to vary the position of the nozzle relative to that of the skimmer while the source is running. This possibility has been used to find a nozzle position which results in an azimuthally symmetric distribution. The achieved symmetric distribution is shown in Fig. 21 and profiles of the atomic hadrogen component in the beam, measured in x and y direction at $z = 567$ mm and $z = 697$ mm, are presented in Fig. 22. Fits by Gaussian distributions to the data yield full widths at half maximum $\Gamma_x = (7.36 \pm 0.43)$ mm, $\Gamma_y = (6.68 \pm 0.80)$ mm for the distributions measured at $z = 567$ mm and $\Gamma_x = (6.69 \pm 0.22)$ mm, $\Gamma_y = (6.38 \pm 0.27)$ mm at 697 mm.

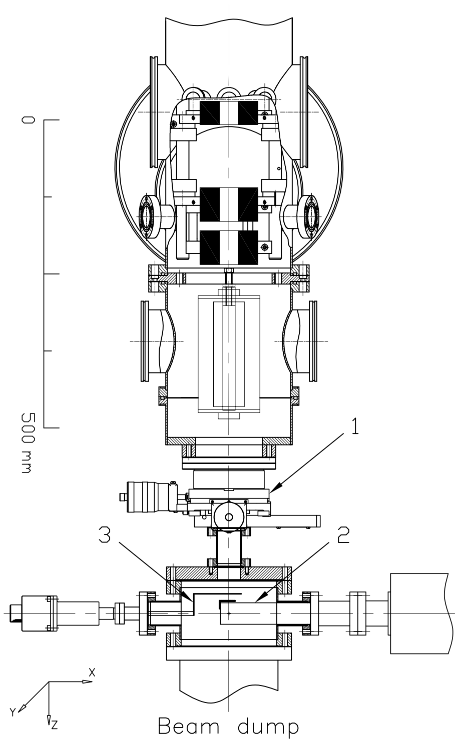

FIG. 19. Setup for the measurements of the beam profile with the QMS. (1): xy-table enabling two-dimensional displacement of the entrance window of the QMS against the geometrical axis of the ABS; (2): the QMS; (3): manually operated beam shutter. The beam dump is an axially mounted cryo pump.

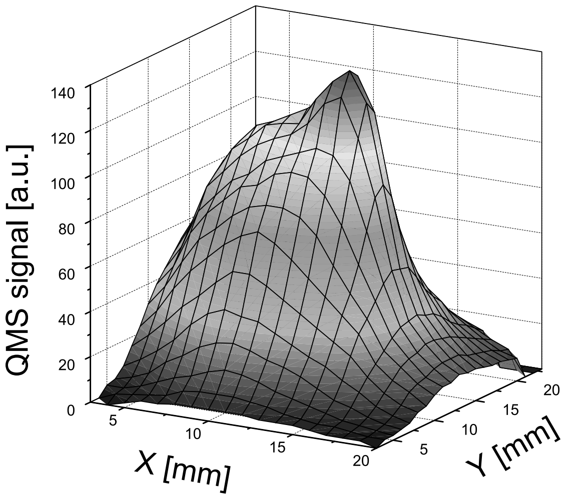

FIG. 20. Two-dimensional distribution of the atomic hydrogen component of the beam at $z = 567$ mm before the nozzle-to-skimmer adjustment, showing a disinct deviation from azimuthal symmetry.

C. Reduction of MoO_3 by hydrogen

In addition to the compression tube and the QMS technique, a supplementary attempt was made to determine the beam profile by exposing molybdenum trioxide (a

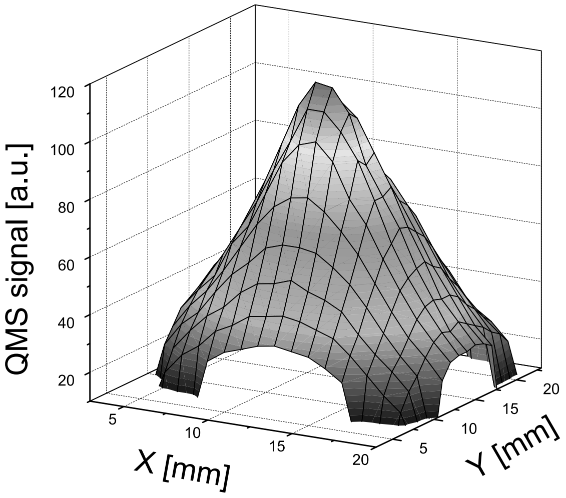

FIG. 21. The distribution corresponding to that of Fig. 20 after nozzle-to-skimmer adjustment resulting in azimuthal symmetry.

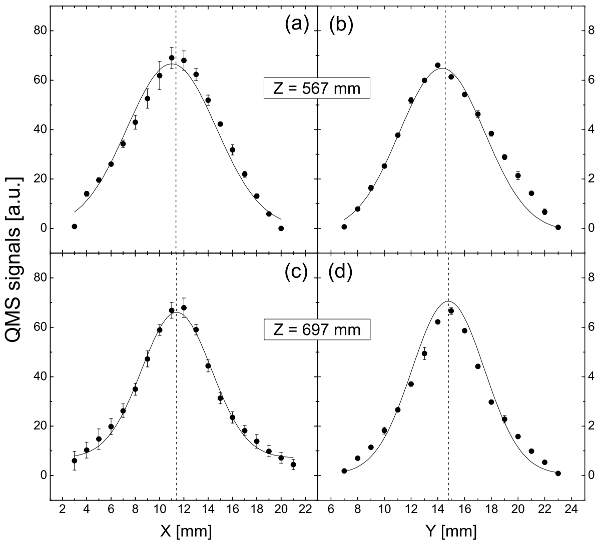

FIG. 22. Profiles of the atomic hydrogen component in the beam, measured with the QMS 567 mm and 697 mm behind the last magnet.

yellowish powder) on a glass plate to the beam. The principle of this method is based on the reduction of MoO_3 to a lower oxide of blue colour. It first was used in the experiment to measure the magnetic moment of the hydrogen atom by splitting of the beam in an inhomogeneous magnetic field [61].

This method is much simpler than the time-consuming measurements described in Secs. V A and V B. It gives qualitative results as presented in Fig. 23. A quantitative analysis, however, requires development of the measuring technique (e.g., preparation of glass plates, study of the optimum exposure time, digital image processing).

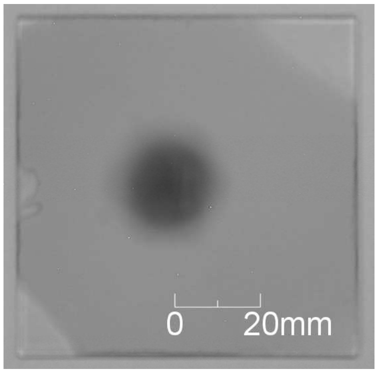

FIG. 23. Photo of the glass plate covered with molybdenum trioxide MoO_3 exposed to the atomic hydrogen beam.

D. Summary of the profile measurements

Table III summarizes results of the measurements of the ABS beam profile with the compression-tube and the QMS setup. The larger errors of the widths, measured with the QMS, are due to the lack of measurements with the dissociator switched off and the necessity to estimate the background signal from the existing data. Within the errors, the measured widths do not show a dependence on the distance from the last magnet. This facilitates to position the feeding tube of the storage cell in a wide range of a distances to the last magnet. The average values $\Gamma_x = (6.38 \pm 0.60)\,\mathrm{mm}$ and $\Gamma_y = (6.84 \pm 0.33)\,\mathrm{mm}$ agree within the errors and yield a common width of $\Gamma_{x,y} = (6.73 \pm 0.29)\,\mathrm{mm}$. The two-dimensional Gaussian distribution of this width allows one to estimate the fraction η of the beam intensity injected into the compression tube or a feeding tube. For a tube of 10 mm diameter $\eta = 0.78 \pm 0.03$, comparable with $\eta \approx 0.7$ given in Sec. V A.

TABLE III. Dimensions (FWHM) of the atomic hydrogen beam measured with the compression tube (CT) and the crossed-beam quadrupole mass spectrometer (QMS) at distances z to the last magnet along perpendicular directions x and y.

	z[mm]	Γ_x[mm]	Γ_y[mm]
CT	300	6.42 ± 0.09	6.99 ± 0.06
CT	337	6.27 ± 0.08	6.58 ± 0.08
QMS	567	7.36 ± 0.43	6.68 ± 0.80
QMS	697	6.69 ± 0.22	6.38 ± 0.27

VI. DEGREE OF DISSOCIATION

Besides the intensity of the atomic beam it is important to determine the molecular fraction in the beam. Molecules injected into the feeding tube, reduce the polarization of the target gas.

A. Measurements with crossed-beam QMS

In addition to the data on the profile of the atomic hydrogen beam (Sec. V B), data on the distributions of molecular hydrogen in the beam were taken, too, at the positions $z = 567$ mm and 697 mm behind the last magnet. The relation between the degree of dissociation and the QMS signals by the atomic and molecular beam component was given above by Eq. (6). The coefficient $k_v = \overline{v}_m/\overline{v}_a$, however, is chosen here under the assumption that the average velocity of the atoms is determined by the nozzle temperature of 65 K and that of the molecules by scattering and recombination on the ABS chamber walls at 290 K. This yields $k_v = \sqrt{2 \cdot 65/290} = 0.67$, in good agreement with Ref.[13], where this coefficient was determined by the measured velocity distributions under similar conditions.

The measured profiles of the atomic fraction (identical to those of Fig. 21), those of the molecular fraction, and those of the degree of dissociation, deduced from Eq. (6), are collected in Fig. 24.

As it is seen from the figure, the distribution of the degree of dissociation shows a dip around the central line due to the higher density of molecular hydrogen originating from the nozzle. The mean value in an aperture of 10 mm diameter results as $\overline{\alpha} = 0.95 \pm 0.04$.

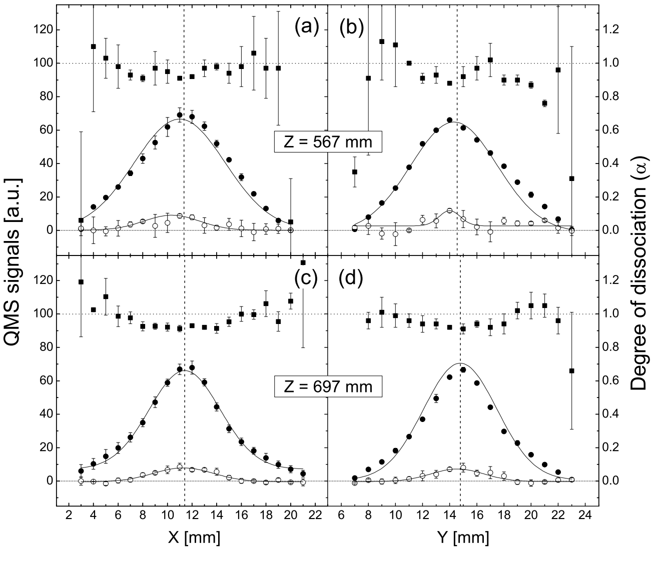

FIG. 24. Spatial distributions of H_1 (●), H_2 (○) and degree of dissociation (■) averaged over 3 mm wide bands in the xz and yz planes, respectively (here the z-axis is the geometrical axis of the ABS).

B. Measurements with the Lamb-shift polarimeter

A cup in the quench chamber of the Lamb-shift polarimeter (LSP), described in Ref.[8], allows one to measure the currents $I_{\mathrm{cup}}(\mathrm{H}_1)$ and $I_{\mathrm{cup}}(\mathrm{H}_2)$ of the H_1^+ and H_2^+ ions, extracted from the ionizer and separated by the Wien filter with the cesium evaporation and the spin filter switched off. The relation between the degree of dissociation α and the measured currents is

$$\alpha = \frac{I_{\mathrm{cup}}(\mathrm{H}_1) - \frac{r_1}{r_2} I_{\mathrm{cup}}(\mathrm{H}_2)}{I_{\mathrm{cup}}(\mathrm{H}_1) - \frac{r_1}{r_2} I_{\mathrm{cup}}(\mathrm{H}_2) + 2\frac{k_v}{r_2} I_{\mathrm{cup}}(\mathrm{H}_2)}. \tag{10}$$

Among the three coefficients, $k_v = 0.67$ as for the measurement with the QMS. For the electron energy of about 100 keV, the ratio r_1 of dissociative to non-dissociative ionization of H_2 is[8]

$$r_1 = \frac{\sigma(\mathrm{H}_2 \to 2\mathrm{H}_1^+)}{\sigma(\mathrm{H}_2 \to \mathrm{H}_2^+)} = 0.095 \pm 0.008 \tag{11}$$

and the ratio between the ionization cross sections is[8,57]

$$r_2 = \frac{\sigma_{\mathrm{ion}}(\mathrm{H}_2)}{\sigma_{\mathrm{ion}}(\mathrm{H}_1)} = 1.7 \pm 0.1. \tag{12}$$

At the standard operation parameters of the source (Sec. IV), the measured currents are $I_{\mathrm{cup}}(\mathrm{H}_1) = (125 \pm 0.5)$ nA and $I_{\mathrm{cup}}(\mathrm{H}_2) = (6.4 \pm 0.1)$ nA, yielding $\bar{\alpha} = (0.96 \pm 0.04)$, in excellent agreement with the value resulting from the measurements with the QMS (Sec. VI A).

VII. BEAM POLARIZATION

The Lamb-shift polarimeter was designed, built, and tested at Universität zu Köln[7]. It was used to measure and to optimize the polarization of the atomic hydrogen and deuterium beams delivered by the ABS. Details are found in Ref.[7].

The vector polarization p_z for hydrogen is defined by the relative hyperfine-state occupation numbers $N(m_I)$,

$$p_z = \frac{N(+\frac{1}{2}) - N(-\frac{1}{2})}{N(+\frac{1}{2}) + N(-\frac{1}{2})}, \tag{13}$$

for deuterium

$$p_z = \frac{N(+1) - N(-1)}{N(+1) + N(0) + N(-1)}. \tag{14}$$

Deuterium tensor polarization p_{zz} is given by

$$p_{zz} = \frac{N(+1) + N(-1) - 2 \cdot N(0)}{N(+1) + N(0) + N(-1)}. \tag{15}$$

These polarizations can be derived from the measured Lyman-α peak strengths S by application of a number of correction factors[7,8].

Typical Lyman α spectra, measured with the polarized hydrogen and deuterium beam from the ABS, are shown in the Figs. 25 and 26.

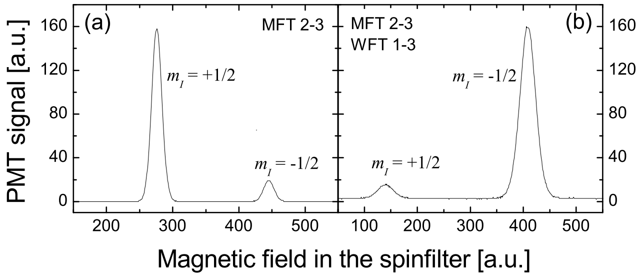

FIG. 25. Lyman-α spectra measured with the polarized hydrogen beam. (a): population change from state $|2\rangle$ to state $|3\rangle$ induced by the MFT unit; (b) same as (a) with subsequent population change from state $|1\rangle$ to state $|3\rangle$ induced by the WFT unit.

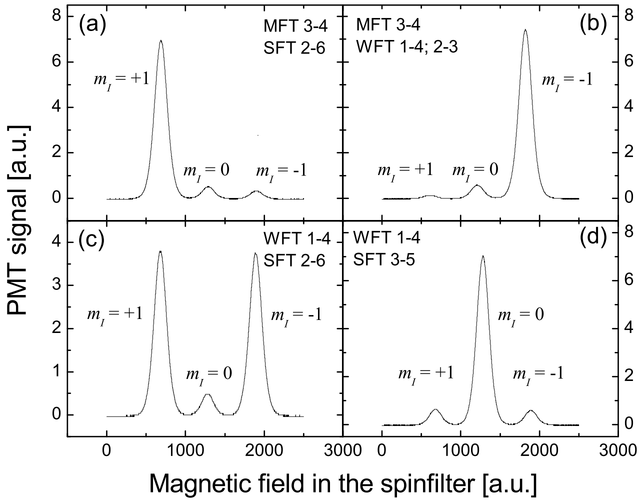

FIG. 26. Lyman-α spectra measured with the polarized deuterium beam. (a) and (b) vector polarization resulting from subsequent transitions MFT ($3 \rightarrow 4$) and SFT ($2 \rightarrow 6$) and WFT ($1 \rightarrow 4, 2 \rightarrow 3$), respectively; (c) and (d) tensor polarization resulting from subsequent transitions WFT ($1 \rightarrow 4$) and SFT ($2 \rightarrow 6$) and SFT ($3 \rightarrow 5$), respectively.

The polarization values for the hydrogen and the deuterium beam, derived from the Lyman-α peak-strength ratios with application of the necessary corrections, are summarized in Table IV.

The vector polarization for hydrogen of the first line reflects the population of state $|1\rangle$ and state $|2\rangle$ according to the Eqs. (3) and (13). The value of 0.91, deduced from the calculated transmission values, is confirmed by the measured one.

TABLE IV. The vector polarization p_z of the hydrogen beam and the vector and the tensor polarization p_{zz} of the deuterium beam from the ABS measured with the Lamb-shift polarimeter.

	populated state(s)	p_z	p_{zz}
Hydrogen	$\|1\rangle$	$+0.89 \pm 0.01$	-
	$\|3\rangle$	-0.96 ± 0.01	-
Deuterium	$\|1\rangle + \|6\rangle$	$+0.88 \pm 0.01$	$+0.88 \pm 0.03$
	$\|3\rangle + \|4\rangle$	-0.91 ± 0.01	$+0.85 \pm 0.02$
	$\|3\rangle + \|6\rangle$	$+0.005 \pm 0.003$	$+0.90 \pm 0.01$
	$\|2\rangle + \|5\rangle$	$+0.005 \pm 0.003$	-1.71 ± 0.03

VIII. CONCLUSIONS AND OUTLOOK

In this paper, we present the detailed description of the major components of the atomic beam source (ABS) for the polarized internal gas target of the magnet spectrometer ANKE in COSY-Jülich. The ABS was built for the purpose of extending the physics program of ANKE from unpolarized and single-polarized investigations with stored beams towards double-polarized experiments[1], thus facilitating nuclear reaction studies involving $\vec{p}\vec{p}$, $\vec{p}\vec{d}$, $\vec{d}\vec{p}$ and $\vec{d}\vec{d}$ initial states.

The mechanical design took into account that at ANKE the source has to be mounted vertically and transversely movable together with the transverse motion of the spectrometer magnet D2. The design of the system of sextupole magnets took advantage of the developments in the field of rare-earth permanent magnets (NdFeB). Dedicated tools and methods were developed to determine and to optimize the source parameters, i.e., intensity, degree of dissociation, and polarization. Special emphasis was put on the measurements of the spatial distributions of the atomic and molecular beam near the focus, where the feeding tube of the storage cell is located. The ABS has been used in a number of investigations at ANKE, the commissioning effort to prepare the target for the use with polarized H is described in Ref.[62]. Performed studies of the deuteron-charge exchange reaction are summarized in Ref.[63,64], studies in near-threshold pion production are reported about in Ref.[65].

The ABS resides at the ANKE target position for a few months per year only, thus during the remaining time it is used for other studies. It had been observed that the nuclear polarization in recombined hydrogen is partially retained after recombination[66], as well as evidence for nuclear tensor polarization in recombined deuterium molecules[67]. In order to investigate this recombination process in more detail, a special setup has been developed in the framework of an ISTC project[68], and the recombination process for different cell-wall coatings, and different polarizations of the injected hydrogen or deuterium atoms as function of cell-wall temperature, strength of the magnetic holding field, and gas pressure in the cell is presently investigated[69–71].

Appendix A: Preparation of Discharge Tubes and Nozzles

1. Tube Treatment

One end of the discharge tube is machined at a 45° angle, while the other is kept flat. Both ends are then remelted and the tubes are tempered at 150 °C. The tubes are further treated according to the procedure described in Ref.[72], which includes successive cleaning with acetone, methanol, distilled water, and subsequent rinsing by a 2:1 acid mixture of concentrated HF (40%) and HCl (32%) for 5 min. The tubes are then flushed by distilled water and dried.

2. Nozzle Treatment

The nozzles are cleaned in an ultrasonic bath of trichlorethylene, acetone, methanol, and finally distilled water, all at 50 °C. Anodizing takes place in sulfuric acid to form a thin layer of Al_2O_3, as described in Ref.[72]. Afterwards they are immersed in distilled water for 30 min at 95 °C.

ACKNOWLEDGMENTS

The authors want to thank O.W.B. Schult, Institut für Kernphysik (IKP), Jülich, who initiated the polarization program of ANKE. Thanks go to the design office, the mechanical workshop, and especially to W.R. Ermer, all IKP. Valuable advice was received from the PINTEX collaboration at IUCF, from the target group at HERMES, especially N. Koch, and from D. Toporkov, BINP, Novosibirsk. The support by V. Koptev, PNPI, Gatchina, who regrettably passed away in January 2012, is gratefully acknowledged. Thanks go also to R. Poprawe and colleagues, Fraunhofer-Institut für Lasertechnik, Aachen, where the encapsulations of the magnets were laser-welded.

[1] A. Kacharava, F. Rathmann, and C. Wilkin, Spin Physics from COSY to FAIR, COSY Experiment Proposal No. **152** (2005). Available under `http://arXiv:nucl-ex/0511028`.

[2] W. Haeberli, in Proc. 2^{nd} Int. Symp. on Polarization Phenomena of Nucleons, Karlsruhe 1965. Eds. P. Huber and H. Schopper, Experientia Supplementum **12**, 64 (Birkhäuser Verlag, 1966).

[3] E. Steffens and W. Haeberli, Rep. Progr. Phys. **66**, 1887 (2003).

[4] S. Barsov et al., Nucl. Instr. and Meth. A **462**, 364 (2001).

[5] R. Maier, Nucl. Instr. and Meth. A **390**, 1 (1997).

[6] K. Grigoryev et al., Proc. 14th International Workshop on Polarized Sources, Targets and Polarimetry (PSTP 2011), 12-16 September 2011, St.Petersburg, Russia, eds. K. Grigoryev, P. Kravtsov and A. Vasilyev, ISBN 978-5-86763-282-3, 61 (2011).

[7] R. Engels et al., Rev. Sci. Instrum. **74**, 4607 (2003).

[8] R. Engels et al., Rev. Sci. Instrum. **76**, 053305 (2005).

[9] T. Wise et al., Nucl. Instr. and Meth. A **336**, 410 (1993).

[10] W.A. Dezarn et al., Nucl. Instr. and Meth. A **362**, 36 (1995).

[11] T. Rinckel et al., Nucl. Instr. and Meth. A **439**, 117 (2000).

[12] F. Stock et al., Nucl. Instr. and Meth. A **343**, 334 (1994).

[13] A. Nass et al., Nucl. Instr. and Meth. A **505**, 633 (2003).

[14] V. Derenchuk et al., Proc. Conf. Polarized Ion Sources and Polarized Gas Targets, Madison, WI, 1993. Eds. L.W. Anderson and W. Haeberli, AIP Conf. Proc. **293**, 72 (American Institute of Physics, 1994).

[15] H. Okamura et al., see Ref.[14], p. 84.

[16] K. Hatanaka et al., Nucl. Instr. and Meth. A **384**, 575 (1997).

[17] Manufacturer Schiffer Metall- & Vakuumtechnik, 52428 Jülich, Germany.

[18] Single-stage type RGS/120, refrigerating capacity 120 W at 80 K and 20 W at 30 K, Leybold Vacuum GmbH, 50968 Köln, Germany.

[19] Mini UHV gate valve, series 010, VAT Germany GmbH, 85630 Grasbrunn, Germany.

[20] Type F3 fomblin oil, Pfeiffer Vacuum GmbH, 35614 Asslar, Germany.

[21] Model HU 1, Leybold Vacuum GmbH, 50968 Köln, Germany.

[22] Manufacturer SK Industriemodell GmbH, 52531 Übach-Palenberg, Germany.

[23] Type PFG 600 RF with automatic matchbox PFM 1500 A-IND, Hüttinger Elektronik GmbH, 79110 Freiburg, Germany.

[24] W. Korsch, PhD Thesis, Philipps Universität Marburg (1990).

[25] F. Stock et al., Int. Workshop on Polarized Beams and Polarized Gas Targets, Koeln, Germany, 1995. Eds. H. Paetz gen. Schieck and L. Sydow (World Scientific Publ. Co., 1996) p. 260.

[26] The first number denotes the outer diameter and the second one the wall thickness.

[27] Type Duran 8330, equivalent to Corning 7740 (Pyrex), Schott AG, 55122 Mainz, Germany.

[28] Ultra-Kryomat RUL 80-D, Lauda Dr. R. Wobser GmbH, 97912 Lauda-Königshofen, Germany.

[29] ODU-Kontakt GmbH, 84444 Mühldorf, Germany.

[30] Handbook of Chemistry and Physics, Ed. R.C. East (The Chemical Rubber Co., 1973), p. E-10.

[31] N. Koch and E. Steffens, Rev. Sci. Instrum. **70**, 1631 (1999).

[32] A. Vassiliev et al., Petersburg Nuclear Physics Institute Report NP-32-1997 No. 2175 (1997).

[33] B. Lorentz, Diploma Thesis, Ruprecht-Karls-Universität Heidelberg (1993).

[34] A. Nass and E. Steffens, Nucl. Instr. and Meth. A **598**, 653 (2009).

[35] W. Haeberli, Ann. Rev. Nucl. Sci. **17**, 373 (1967).

[36] A. Vassiliev et al., Rev. Sci. Instr., **71**, 3331 (2000).

[37] W. Kubischta, Proc. Workshop on Polarized Gas Targets for Storage Rings, Heidelberg, 23-26 September 1991, Eds. H.G. Gaul, E. Steffens, and K. Zapfe (Max-Planck-Institut für Kernphysik Heidelberg).

[38] The labeling of the hyperfine states as $|1\rangle = |m_j = +1/2, m_I = +1/2\rangle$, $|2\rangle = |+1/2, -1/2\rangle$, $|3\rangle = |-1/2, +1/2\rangle$, and $|4\rangle = |-1/2, -1/2\rangle$ for hydrogen and $|1\rangle = |+1/2, +1\rangle$, $|2\rangle = |+1/2, 0\rangle$, $|3\rangle = |+1/2, -1\rangle$, $|4\rangle = |-1/2, -1\rangle$, $|5\rangle = |-1/2, 0\rangle$, and

$|6\rangle = |-1/2, +1\rangle$ for deuterium follows that of Ref.[35].

[39] Produced from VACODYM 510HR, 383HR, and 400HR by Vacuumschmelze GmbH, 63412 Hanau, Germany.

[40] K. Halbach, Nucl. Instr. and Meth. **169**, 1 (1980).

[41] Welding performed at Fraunhofer-Institut für Lasertechnik, 52074 Aachen, Germany.

[42] A. Abragam and J.M. Winter, Phys. Rev. Lett. **1**, 374 (1958).

[43] S. Lorenz, Diploma Thesis, Friedrich-Alexander-Universität Erlangen-Nürnberg (1999).

[44] H.-G. Gaul and E. Steffens, Nucl. Instr. and Meth. A **316**, 297 (1992).

[45] S. Oh, Nucl. Instr. and Meth. **82**, 189 (1970).

[46] H. Paetz gen. Schieck, Nucl. Instr. and Meth. A **587**, 213 (2008).

[47] R.J. Philpott, Nucl. Instr. and Meth. A **259**, 317 (1987).

[48] H. Jänsch et al., Hyperfine Interactions **22**, 253 (1985).

[49] A.D. Roberts et al., Nucl. Instr. and Meth. A **322**, 6 (1992).

[50] M. Capiluppi et al., `http://theor.jinr.ru/~spin2012/talks/s6/Steffens.pdf` (to be published in Physics of Elementary Particles and Atomic Nuclei, JINR, Russia, `http://pepan.jinr.ru/pepan/eng/about/`).

[51] Manufactured by St. Petersburg Nuclear Physics Institute, 188300 Gatchina, Russia.

[52] H. Kleines et al., Nucl. Instr. Meth. A **560**, 503 (2006).

[53] A. Vassiliev et al., Petersburg Nuclear Physics Institute Report EP-46-1998 No. 2260 (1998).

[54] A. Vassiliev et al., Proc. Int. Workshop Polarized Sources and Targets, Erlangen, Germany, September 29 -October 2, 1999. Eds. A. Gute, S. Lorenz, E. Steffens (Universität Erlangen-Nürnberg, 1999), p. 200.

[55] M. Mikirtytchiants, Diploma Thesis, St. Petersburg State Technical University (1999).

[56] M. Mikirtytchiants et al., see Ref.[54], p. 478.

[57] Y.K. Kim et al., Electron-impact cross section database, 2002, `http://pysics.nist.gov/PhysRefData/Ionization`.

[58] M. Nekipelov, Diploma Thesis, St. Petersburg State Technical University (1999).

[59] M. Nekipelov et al., see Ref.[54], p. 486.

[60] A. Roth, Vacuum Technology (Elsevier, Amsterdam, 1996).

[61] T.E. Phipps and J.B. Taylor, Phys. Rev. **29**, 309 (1927).

[62] M. Mikirtychyants et al., J. Phys.: Conf. Ser. 295, 012148 (2011).

[63] D. Mchedlishvili et al., J. Phys.: Conf. Ser. 295, 012099 (2011).

[64] F. Rathmann, J. Phys.: Conf. Ser. 295, 012006 (2011).

[65] S. Dymov (for the ANKE collaboration), J. Phys.: Conf. Ser. 295, 012095 (2011).

[66] T. Wise et al., Phys. Rev. Lett. **87**, 042701 (2001).

[67] J.F.J. van den Brand et al., Phys. Rev. Lett. **78**, 1235 (1997).

[68] International Science and Technology Center, Project No. 1861.

[69] Work now financed by Deutsche Forschungsgemeinschaft, project 436 RUS 113/977/01.

[70] R. Engels et al., Proc. 13th Int. Workshop on Polarized Sources, Targets and Polarimetry, Ferrara, Italy, September 7-11, 2009. Eds. G. Ciullo, M. Contalbrigo, P. Lenisa (World Scientific, 2011), p. 215.

[71] R. Engels et al., J. Phys.: Conf. Ser. 295, 012161 (2011).

[72] N. Koch, PhD Thesis, Friedrich-Alexander-Universität Erlangen-Nürnberg (1999).